

Harmonic surface mapping algorithm for a dielectric sphere immersed in electrolytes

Jing Fu,¹ Zecheng Gan,^{2,*} and Zhenli Xu^{1,†}

¹*School of Mathematical Sciences, Institute of Natural Sciences,
and MoE Key Lab of Scientific and Engineering Computing,
Shanghai Jiao Tong University, Shanghai 200240, China*

²*Department of Mathematics, University of Michigan,
Ann Arbor, Michigan 48109, U.S.A.*

(Dated: May 25, 2022)

Abstract

A harmonic surface mapping algorithm (HSMA) is presented for accurately solving the linearized Poisson–Boltzmann equation for a dielectric sphere immersed in electrolytes. By introducing an auxiliary spherical surface, we formulate the electrostatic *reaction potential* into the sum of image charges and a local spherical harmonic expansion. Green’s second identity is further used to transform the local expansion into an integral on the auxiliary surface. Finally, we apply the Fibonacci integration scheme to discretize the surface integral, which again becomes a sum of discrete image charges. Combined with the fast multipole method, our algorithm allows fast and accurate simulation for a dielectric sphere immersed in electrolytes. We demonstrate the accuracy and efficiency of our algorithm through a few concrete numerical examples. We also examine the challenging case of a source charge very close to the dielectric interface, where the method still converges very well owing to the analytical resolving of singularity with the image charges. Thus, our method provides an attractive way for large-scale simulations of charged particles in electrolytes.

*Electronic address: zecheng@umich.edu

†Electronic address: xuzl@sjtu.edu.cn

I. INTRODUCTION

Electrostatic effect is ubiquitous in nature, and have caught much attention in theoretical and numerical investigations of charged biomolecular systems [1–3]. Specifically, accurate representation of the electrolyte solvent is essential for modeling and simulations of biomolecules, which have aroused widespread concern up to the present [4–10].

The explicit solvent model [11, 12], where the solvent is represented explicitly with discrete ions and water molecules, provides accurate description of the solvent. However, its application becomes limited due to the expensive computational cost. The implicit solvent model [13–16] replaces the atomic details of the solvent with a dielectric continuum, by taking the so-called mean-field approximation of the electrolyte solvent. Such model can dramatically save the computational cost, but the detailed electrostatic interaction between the water molecules/ions and the biomolecule is ignored. An alternative that taking advantage of both models is the hybrid explicit/implicit model [17, 18]. The hybrid model introduces a spherical cavity which encloses the biomolecule together with its nearby surrounding solvent. Inside the spherical cavity, both the solute and solvent are modeled explicitly, while in the bulk region away from the biomolecule, the solvent is treated implicitly using the linearized Poisson–Boltzmann (LPB) equation [19–22]. The hybrid model can accurately model the solvent-solute interaction near the bimolecular surface, and also significantly reduce the degree of freedom in molecular simulations. However, after introducing the spherical cavity, one needs to numerically solve for the *reaction potential* inside the cavity due to the implicit solvent outside. Thus for the hybrid model, it is very important to improve the performance in solving the LPB equation in the presence of a dielectric spherical interface.

To solve the reaction potential for such hybrid model, several methods have been proposed. Kirkwood derived the analytical solution of the reaction potential, i.e., the Kirkwood series expansion [23, 24]. However, for large-scale simulations, the performance of this method is not satisfactory due to the slow convergence of the series when ions are close to the interface. A more efficient approach is to combine the analytical image charge method [25, 26] with the fast multipole method (FMM) [27–30]: a high-order accurate image charge method has been developed over recent years [31, 32], which has been successfully applied to multi-scale Monte Carlo simulations of monovalent electrolyte [33].

In this paper, we extend a recently proposed new method, namely, the harmonic surface

mapping algorithm (HSMA) [35] for solving the LPB equation for a dielectric sphere in electrolytes. The HSMA has recently been proposed for fast Coulomb summation, but not yet applied in the hybrid model. The idea of the HSMA is to transform the Kirkwood expansion solution into a surface integral on an auxiliary surface. Applying the high-order Fibonacci integration scheme, the surface integral will be discretized into a sum of image charges. Further combined with FMM, the reaction potential can be calculated both accurately and efficiently with $\mathcal{O}(N)$ complexity. Our numerical results demonstrate that the HSMA can achieve much higher accuracy than the Kirkwood series expansion given the same truncated expansion order p . We also examine the challenging case of a source charge very close to the dielectric interface, where the HSMA still converges very well owing to the analytical resolving of singularity with the image charges. Thus we expect the HSMA to be a very useful tool in large-scale simulations of physical/biological systems under the hybrid model.

The rest of the paper is organized as follows. We describe the model and derivation of the HSMA in Sec. II. The resulting algorithm, its computational complexity and error analysis are summarized in Sec. III. Then numerical results are given in Sec. IV, where the accuracy and efficiency performance are demonstrated through a few concrete examples. Finally, our conclusion and future works are summarized in Sec. V.

II. METHOD

A. Model and mathematical formulations

Consider a set of N point sources locating at $\mathbf{x}_i = (r_i, \theta_i, \phi_i)$ inside a spherical domain $\Omega_1 \in \mathbb{R}^3$, each carrying charge q_i , while the outside solvent domain Ω_2 is modeled as a dielectric continuum, as is illustrated in Fig. 1. Then for the hybrid model, the electrostatic potential at $\mathbf{x} = (r, \theta, \phi)$ satisfies

$$-\nabla \cdot \varepsilon_1 \nabla \Phi_1(\mathbf{x}) = 4\pi \sum_{i=1}^N q_i \delta(\mathbf{x} - \mathbf{x}_i), \text{ in } \Omega_1, \quad (1)$$

$$-\nabla^2 \Phi_2(\mathbf{x}) + \kappa^2 \Phi_2(\mathbf{x}) = 0, \text{ in } \Omega_2, \quad (2)$$

where $\Phi_1(\mathbf{x})$ and $\Phi_2(\mathbf{x})$ are the electrostatic potential in Ω_1 and Ω_2 , which satisfy the electrostatic interface conditions at $\partial\Omega_1$:

$$\Phi_1 = \Phi_2, \quad \varepsilon_1 \frac{\partial \Phi_1}{\partial r} = \varepsilon_2 \frac{\partial \Phi_2}{\partial r}, \text{ for } \mathbf{x} \in \partial\Omega_1. \quad (3)$$

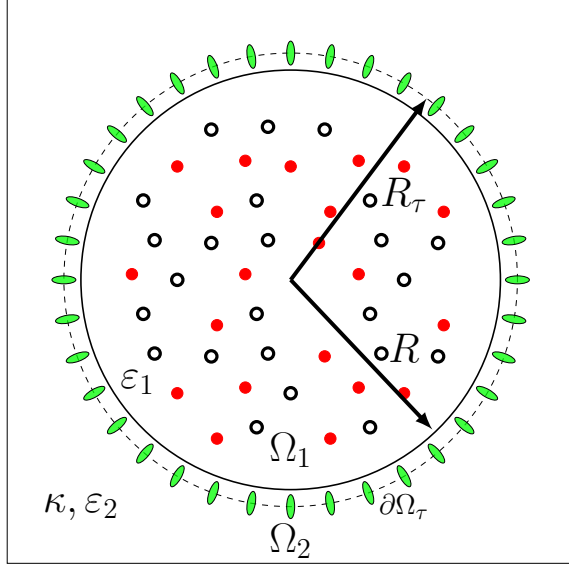


FIG. 1: 2D schematic illustration for a dielectric sphere immersed in an electrolyte. Ω_1 is the inside domain of the dielectric sphere, which contains explicit source charges. Ω_2 is the exterior domain, where the solvent is described as a dielectric continuum. The dashed surface $\partial\Omega_\tau$ is an auxiliary surface enclosing Ω_1 . In the HSMA, the reaction potential due to the continuum solvent outside $\partial\Omega_\tau$ is represented by point/dipole images locating on it.

Note that $\varepsilon_1, \varepsilon_2$ are the dielectric constants in Ω_1 and Ω_2 , respectively. κ is the inverse Debye length, $\kappa = (4\pi l_B \sum_j \lambda_j z_j^2)^{1/2}$, where index j runs over all the ion species, and λ_j and z_j are the bulk concentration and valence of the j th ion species. l_B is the solvent Bjerrum length, $l_B = 7.14\text{\AA}$ for water at room temperature. The far-field boundary condition is $\Phi_2 \rightarrow 0$ as $r \rightarrow \infty$.

B. Kirkwood series expansion revisited

We first revisit the Kirkwood series expansion [23, 24] for solving Eqs. (1)–(3). The potential Φ_1 inside Ω_1 can be written as the sum of two contributions,

$$\Phi_1(\mathbf{x}) = \Phi_{\text{Coul}}(\mathbf{x}) + \Phi_{\text{RF}}(\mathbf{x}), \quad (4)$$

where Φ_{Coul} is the Coulomb potential due to the point source charges,

$$\Phi_{\text{Coul}}(\mathbf{x}) = \sum_{i=1}^N \frac{q_i}{4\pi\varepsilon_1|\mathbf{x} - \mathbf{x}_i|}. \quad (5)$$

One can further expand the Coulomb potential using spherical harmonics [36], obtaining the following expression for Φ_{Coul} :

$$\Phi_{\text{Coul}}(\mathbf{x}) = \sum_{i=1}^N \sum_{n=0}^{\infty} \sum_{m=-n}^n \frac{q_i}{(2n+1)\varepsilon_1} \frac{r_{<}^n}{r_{>}^{n+1}} Y_n^{m*}(\theta_i, \phi_i) Y_n^m(\theta, \phi), \quad (6)$$

where $r_{<}(r_{>})$ is the smaller (larger) value between r_i and r , and $Y_n^m(\theta, \phi)$ is the spherical harmonic function of degree n and order m . Note that the superscript $*$ denotes complex conjugate. The second contribution Φ_{RF} is the reaction potential due to the exterior continuum solvent. Since Φ_{RF} is a harmonic function, it can also be expanded in terms of spherical harmonics,

$$\Phi_{\text{RF}}(\mathbf{x}) = \sum_{n=0}^{\infty} \sum_{m=-n}^n A_n^m r^n Y_n^m(\theta, \phi), \quad (7)$$

where A_n^m are the undetermined expansion coefficients.

Analogously, the potential Φ_2 in the exterior region Ω_2 can also be expanded as,

$$\Phi_2(\mathbf{x}) = \sum_{n=0}^{\infty} \sum_{m=-n}^n B_n^m k_n(\kappa r) Y_n^m(\theta, \phi), \quad (8)$$

where B_n^m are unknown coefficients and $k_n(\cdot)$ is the modified spherical Hankel function of order n , defined as [37]:

$$k_n(\mu) = \frac{\pi e^{-\mu}}{2\mu} \sum_{l=0}^n \frac{(n+l)!}{l!(n-l)!} \frac{1}{(2\mu)^l}. \quad (9)$$

Now since both Φ_1 and Φ_2 are expanded using spherical harmonics, we can further substitute Eqs. (4)–(8) into the interface conditions Eq. (3) to solve for the unknown coefficients A_n^m and B_n^m . By the orthogonality of the spherical harmonics, we obtain the following expressions for A_n^m and B_n^m ,

$$A_n^m(\mu) = \frac{\varepsilon(n+1)S_n(\mu) + 1}{\varepsilon n S_n(\mu) - 1} \sum_{i=1}^N \frac{q_i}{(2n+1)\varepsilon_1 R} \frac{Y_n^{m*}(\theta_i, \phi_i)}{r_{\text{K},i}^n}, \quad (10)$$

$$B_n^m(\mu) = \frac{\varepsilon(2n+1)}{\varepsilon n k_n(\mu) - \mu k_n'(\mu)} \sum_{i=1}^N \frac{q_i}{(2n+1)\varepsilon_1 R} \left(\frac{r_i}{R}\right)^n Y_n^{m*}(\theta_i, \phi_i), \quad (11)$$

where $\mathbf{r}_{\text{K},i}$ is the so-called Kelvin image point, defined as $\mathbf{r}_{\text{K},i} = (R/r_i)^2 \mathbf{x}_i$, and $\varepsilon = \varepsilon_1/\varepsilon_2$, $\mu = \kappa R$ and $S_n(\mu) = \frac{k_n(\mu)}{\mu k_n'(\mu)}$.

Finally, it is worth noting that $S_n(\mu)$ has the following asymptotic approximations, as $\mu \rightarrow \infty$ [32, 38],

$$S_n(\mu) = -\frac{1}{n+1+\mu} + \mathcal{O}\left(\frac{1}{\mu^2}\right), \quad \mu \rightarrow \infty, \quad (12)$$

and as $\mu \rightarrow 0$,

$$S_n(\mu) = -\frac{1}{n+1+\mu} + \mathcal{O}(\mu), \quad \mu \rightarrow 0, \quad (13)$$

thus the formula gives correct leading-order asymptotics for both low and high concentrations of the electrolytes. With the asymptotic formulas, the reaction potential can be further simplified into an image charge expression, which will be described in Sec. II C.

C. Image charge representation

In this section, we derive an image charge representation for the reaction potential. First, consider the expansion coefficients of $A_n^m(\mu)$ in Eq. (10), denoted here as $M_n(\mu)$:

$$M_n(\mu) = \frac{\varepsilon(n+1)S_n(\mu) + 1}{\varepsilon n S_n(\mu) - 1}. \quad (14)$$

By substituting the asymptotic formula (i.e. Eq. (12)) into Eq. (14), $M_n(\mu)$ can be decomposed into three parts:

$$M_n(\mu) = \gamma + \frac{\bar{\delta}}{n+\sigma} + \widehat{M}_n(\mu), \quad (15)$$

where

$$\gamma = \frac{\varepsilon - 1}{\varepsilon + 1}, \quad \sigma = \frac{1 + \mu}{1 + \varepsilon}, \quad \bar{\delta} = \gamma(1 - \sigma) - \frac{\mu}{1 + \varepsilon}, \quad (16)$$

and

$$\widehat{M}_n(\mu) = M_n(\mu) - \gamma - \frac{\bar{\delta}}{n+\sigma}. \quad (17)$$

Note that $\widehat{M}_n(\mu)$ consists of higher-order terms in the asymptotic expansion, which vanishes as $n \rightarrow \infty$.

Next, substitute Eq. (15) into Eqs. (7) and (10), and further apply the following identity,

$$\frac{\bar{\delta}}{n+\sigma} = r_{\text{K},i}^{n+\sigma} \int_{r_{\text{K},i}}^{\infty} \frac{\bar{\delta}}{x^{n+\sigma+1}} dx, \quad (18)$$

which is valid for all $n \geq 0$ with $\sigma > 0$. We arrive at the following expression for the reaction potential Φ_{RF} as the sum of Kelvin images, line image densities, and a spherical harmonic expansion which can be regarded as a higher-order correction term:

$$\Phi_{\text{RF}}(\mathbf{x}) = \underbrace{\sum_{i=1}^N \frac{q_i \gamma r_{\text{K},i}}{4\pi\varepsilon_1 R |\mathbf{x} - \mathbf{r}_{\text{K},i}|}}_{\text{Kelvin images}} + \underbrace{\sum_{i=1}^N \int_{r_{\text{K},i}}^{\infty} \frac{q_i \bar{\delta} (t/r_{\text{K},i})^{-\sigma}}{4\pi\varepsilon_1 R |\mathbf{x} - \mathbf{t}|} dt}_{\text{Line image densities}}$$

$$+ \underbrace{\sum_{i=1}^N \sum_{n=0}^{\infty} \sum_{m=-n}^n \frac{q_i}{(2n+1)\varepsilon_1 R} \left(\frac{r}{r_{\mathbf{K},i}}\right)^n \widehat{M}_n(\mu) Y_n^{m*}(\theta_i, \phi_i) Y_n^m(\theta, \phi)}_{\text{Higher-order correction term}}. \quad (19)$$

In [32], numerical results show that just keeping the first two leading-order terms can approximate the reaction potential accurately when the source charges are *not* very close to the dielectric interface. In this work, we aim to keep the third correction term, which will allow us to obtain high-order accuracy even when source charges are close to the interface. And since direct calculation of the correction term is very time consuming, we introduce the harmonic surface mapping technique below to further simplify it as a sum of images.

D. Harmonic surface mapping

The harmonic surface mapping algorithm is a recently proposed fast algorithm [35] for solving the Poisson equation with either periodic/non-periodic boundary conditions. But it has not yet been applied to such hybrid model, where one needs to solve the LPB equation and there exists a spherical dielectric interface.

Now let us introduce the auxiliary spherical surface $\partial\Omega_\tau$. As was shown in Fig. 1, it is concentric with $\partial\Omega_1$ and encloses the whole interior domain Ω_1 . The radius of the auxiliary surface is $R_\tau = (1+\tau)R$, note that R is the radius of Ω_1 and we have an adjustable parameter $\tau > 0$ (practically setting the value of τ will be discussed in Sec. IV). Then the line image integral can be divided as

$$\int_{r_{\mathbf{K},i}}^{\infty} = \int_{r_{\mathbf{K},i}}^{R_\tau} + \int_{R_\tau}^{\infty}. \quad (20)$$

We use the trapezoidal rule to approximate the first line integral on $[r_{\mathbf{K},i}, R_\tau]$, then the quadrature weight assigned at the Kelvin point $\mathbf{r}_{\mathbf{K},i}$ is $\bar{\delta} \frac{(R_\tau - r_{\mathbf{K},i}) q_i}{2R}$. Note that its location overlaps with the original Kelvin image, so we just modify the original Kelvin image and obtain the new Kelvin image magnitude

$$q_{\mathbf{K},i} = \frac{q_i}{R} \left[\gamma r_{\mathbf{K},i} + \bar{\delta} \frac{(R_\tau - r_{\mathbf{K},i})}{2} \right]. \quad (21)$$

The other trapezoidal point at \mathbf{R}_τ and the numerical discretization error can be both absorbed into the correction term, thus we define the modified harmonic coefficient $\widehat{M}'_n(\mu)$,

$$\widehat{M}'_n(\mu) = M_n(\mu) - \gamma - \bar{\delta} \frac{(R_\tau - r_{\mathbf{K},i})}{2r_{\mathbf{K},i}}. \quad (22)$$

Then the reaction potential Φ_{RF} can be rewritten as,

$$\Phi_{\text{RF}}(\mathbf{x}) = \sum_{i=1}^N \frac{q_{\text{K},i}}{4\pi\varepsilon_1|\mathbf{x} - \mathbf{r}_{\text{K},i}|} + \sum_{i=1}^N \sum_{n=0}^{\infty} \sum_{m=-n}^n \frac{q_i \widehat{M}'_n(\mu)}{(2n+1)\varepsilon_1 R} \left(\frac{r}{r_{\text{K},i}}\right)^n Y_n^{m*}(\theta_i, \phi_i) Y_n^m(\theta, \phi). \quad (23)$$

It worths noting that though the trapezoidal rule is used to obtain the modified Kelvin image magnitude $q_{\text{K},i}$, the above expression for Φ_{RF} is still exact. However, directly calculating the second correction term in Eq. (23) will again be time consuming, so we discuss below how to handle it computationally through the HSMA approach.

We first define the correction term in Eq. (23) (truncated at order p) as

$$\Phi_{\text{corr}}(\mathbf{x}) \approx \sum_{n=0}^p \sum_{m=-n}^n \widehat{A}_n^m r^n Y_n^m(\theta, \phi), \quad (24)$$

where

$$\widehat{A}_n^m = \sum_{i=1}^N \frac{q_i \widehat{M}'_n(\mu)}{(2n+1)\varepsilon_1 R} \frac{Y_n^{m*}(\theta_i, \phi_i)}{r_{\text{K},i}^n}. \quad (25)$$

Through the Green's second identity [35] and the fact that Φ_{corr} is a harmonic function, one can convert Φ_{corr} into a surface integral on the auxiliary surface $\partial\Omega_\tau$,

$$\Phi_{\text{corr}}(\mathbf{x}) = \oint\!\!\!\oint_{\partial\Omega_\tau} \left[G(\mathbf{x}, \mathbf{y}) \frac{\partial\Phi_{\text{corr}}(\mathbf{y})}{\partial\nu_y} - \Phi_{\text{corr}}(\mathbf{y}) \frac{\partial G(\mathbf{x}, \mathbf{y})}{\partial\nu_y} \right] dS_y, \quad (26)$$

where $G(\mathbf{x}, \mathbf{y}) = \frac{1}{4\pi|\mathbf{x}-\mathbf{y}|}$ is the Green's function for Poisson equation in free space and ν_y is the unit outward normal vector at \mathbf{y} . We further use the central difference scheme to approximate $\frac{\partial G}{\partial\nu_y}$ in Eq. (26), i.e.,

$$\frac{\partial G}{\partial\nu_y} \approx \frac{1}{\Delta y} [G(\mathbf{x}, \mathbf{y}^+) - G(\mathbf{x}, \mathbf{y}^-)], \quad (27)$$

where $\mathbf{y}^\pm = (y \pm \Delta y/2, \theta, \phi)$ and Δy is the central difference step size. Then $\Phi_{\text{corr}}(\mathbf{x})$ can be expressed as the sum of three surface integrals,

$$\Phi_{\text{corr}}(\mathbf{x}) \approx \oint\!\!\!\oint_{\partial\Omega_\tau} \frac{\partial_y \Phi_{\text{corr}}(\mathbf{y})}{4\pi|\mathbf{x}-\mathbf{y}|} dS_y + \oint\!\!\!\oint_{\partial\Omega_\tau^-} \frac{\Phi_{\text{corr}}(\mathbf{y})/\Delta y}{4\pi|\mathbf{x}-\mathbf{y}^-|} dS_y - \oint\!\!\!\oint_{\partial\Omega_\tau^+} \frac{\Phi_{\text{corr}}(\mathbf{y})/\Delta y}{4\pi|\mathbf{x}-\mathbf{y}^+|} dS_y. \quad (28)$$

The first term represents a surface charge density, while the second and third terms are essential a central difference approximation for a surface dipole density. It worths noting that since $\mathbf{x} \in \Omega_1$ while $\mathbf{y} \in \partial\Omega_\tau$, all three integrands in Eq. (28) are non-singular. Thus

the Fibonacci numerical integration scheme [39] can be applied, which achieves $\mathcal{O}(N_\tau^{-6})$ convergence for N_τ discretized grid points.

Suppose $f(\mathbf{y})$ is a non-singular integrand, the Fibonacci integration method discretizes the surface integral over $f(\mathbf{y})$ on a sphere $\partial\Omega_\tau$ as

$$\oint_{\partial\Omega_\tau} f(\mathbf{y})dS_y \approx \frac{2\pi R_\tau^2}{F_2} \sum_{j=0}^{F_2} [1 + \cos(\pi z_j)][f(\mathbf{y}_{2j+1}) + f(\mathbf{y}_{2j+2})], \quad (29)$$

where $z_j = (-1 + 2j/F_2)$, $\mathbf{y}_{2j+1} = (R_\tau, \arccos(z_j + \sin(\pi z_j)/\pi), \pi j F_1/F_2)$, $\mathbf{y}_{2j+2} = (R_\tau, \arccos(z_j + \sin(\pi z_j)/\pi), \pi + \pi j F_1/F_2)$, and $F_1 < F_2$ are two successive Fibonacci numbers. Therefore, after discretization using the Fibonacci integration scheme, Eq. (28) can be approximated by a sum of discrete images located on Ω_τ and Ω_τ^\pm , i.e.,

$$\Phi_{\text{corr}}(\mathbf{x}) \approx \sum_{j=1}^{N_\tau} \frac{\bar{q}_j}{|\bar{\mathbf{y}}_j - \mathbf{x}|}, \quad (30)$$

where $N_\tau = 6(F_2 + 1)$ is the total number of images, and $\bar{q}_j, \bar{\mathbf{y}}_j$ are the charge and location from the Fibonacci numerical integration. Notably, N_τ is independent from the total number of sources N . Finally, we substitute Eq. (30) to the reaction potential Eq. (23) and combine it with the Kelvin images, then obtain a simple expression for Φ_{RF} as a Coulomb sum of $N + N_\tau$ image charges, i.e.,

$$\Phi_{\text{RF}}(\mathbf{x}) \approx \sum_{j=1}^{N+N_\tau} \frac{Q_j}{|\mathbf{Y}_j - \mathbf{x}|}, \quad (31)$$

where $Q_j = q_{\text{K},j}, Y_j = \mathbf{r}_{\text{K},j}$ for $j = 1, \dots, N$, and $Q_j = \bar{q}_j, Y_j = \bar{\mathbf{y}}_j$ for $j = N + 1, \dots, N + N_\tau$.

III. ALGORITHM, COMPLEXITY AND ERROR ANALYSIS

The harmonic surface mapping algorithm steps and its computational complexity are summarized in Algorithm 1.

The numerical error of HSMA comes from three parts. (a). The p -th order truncation error of the spherical harmonic expansion in Eq. (23). An error estimation for this part was given in [40], i.e., if truncated at order p , the truncation error $\mathcal{E}_{\text{trunc}} \sim \mathcal{O}(\frac{1}{1+\tau})^p$; (b). The discretization error from the central difference in Eq. (27) for calculating $\partial G/\partial \nu_y$, $\mathcal{E}_{\text{diff}} \sim \mathcal{O}(\Delta y^2)$; (c). The Fibonacci numerical integration error, $\mathcal{E}_{\text{Fibo}} \sim \mathcal{O}(N_\tau^{-6})$. In practice, we find that the truncation error from part (a) is the dominant part, as long as a reasonable

Algorithm 1 Harmonic surface mapping algorithm

Require: Spherical harmonic expansion truncated order p , dielectric constants $\varepsilon_{1,2}$ and inverse

Debye length κ for the electrolyte, dielectric sphere radius R , auxiliary surface radius $R_\tau = (1 + \tau)R$, source charge locations r_i and charge magnitudes q_i for $i = 1, \dots, N$.

- 1: Construct $2p$ Gauss-Legendre quadrature nodes along θ direction and $2p$ equi-spaced weights along ϕ direction on $\partial\Omega_1$, which will be used for the spherical harmonic transform.
 - 2: Use FMM to calculate the potential generated by the source charges at the quadrature nodes on $\partial\Omega_1$. This step has complexity $\mathcal{O}(N + p^2)$.
 - 3: Discrete spherical harmonic transformation is performed to obtain the spherical harmonic expansion coefficients $\widehat{A}_n^m(\mu)$. This step requires $\mathcal{O}(Np^3)$ operations.
 - 4: Generate the Kelvin image charges $q_K, \mathbf{r}_{K,i}, i = 1, \dots, N$ inside Ω_τ and the Fibonacci integration points and weights $Q_j, \mathbf{R}_j, j = 1, \dots, N_\tau$ on $\partial\Omega_\tau$. This step has complexity $\mathcal{O}(N + N_\tau p^2)$.
 - 5: Use FMM to evaluate the electrostatic potential/field at source charge locations. This step costs $\mathcal{O}(N + N_\tau)$.
-

Δy and N_τ is chosen, the errors from part (b) and (c) are minor. However, it worths noting that given the same truncation order p , the HSMA can achieve better accuracy than merely using the Kirkwood series, due to the fact that the numerical singularity is mainly caused by the Kelvin images, which has been handled here analytically. We will show numerical evidence in Sec. IV.

IV. NUMERICAL RESULTS

In this section, we test the performance of the HSMA in terms of both accuracy and efficiency. In all the calculations, we fix $R = 1, \mu = 5, \varepsilon_1 = 2$ and $\varepsilon_2 = 80$, and vary the parameters τ and p to check the accuracy. Since the error from the central difference is minor, we take the step size to be $\Delta y = 10^{-5}R_\tau$. And we take the results from the Kirkwood series truncated at sufficient large p (for the worst case here we take $p = 201$) as the reference solution.

A. Accuracy tests

We test the accuracy of the HSMA by considering a unit source charge inside the spherical dielectric interface. Suppose a unit point source locating at $\mathbf{x}_s = (r_s, \theta_s, \phi_s)$, we consider the error in its self energy, the self energy E_{self} is defined as

$$E_{\text{self}} = \frac{1}{2} \Phi_{\text{RF}}(\mathbf{x}_s, \mathbf{x}_s). \quad (32)$$

We first investigate the error dependence on the adjustable parameter τ . In Fig. 2 (a), we show the numerical error in E_{self} as a function of the source charge location r_s with $\tau = 0.05, 0.1$ and 0.15 , while fixing $p = 30$ and $F_2 = 1597$. We observe that for r_s ranging from 0

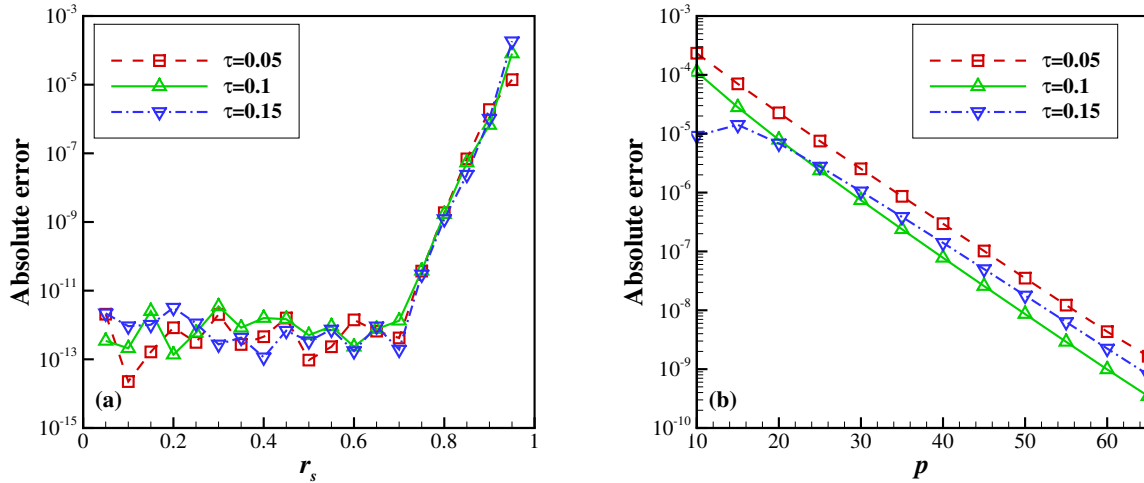


FIG. 2: (a) Absolute errors of the self energy as a function of source charge position r_s for $\tau = 0.05, 0.1$ and 0.15 , we fix $p = 30$ and $F_2 = 1597$. (b) Absolute errors of the self energy as a function of truncated order p for $\tau = 0.05, 0.1$ and 0.15 with $r_s = 0.9$, we fix

$$F_2 = 6765.$$

to 0.95, the error is not very sensitive about the value of τ . As expected, we see that the error increases a few orders of magnitudes as the charge approaches the interface. But even when $r_s = 0.95$, the HSMA can still obtain absolute error $\sim 10^{-4}$. In Fig. 2 (b), we also test the error in E_{self} as a function of the truncated order p for the same set of values for τ . Consistently, we find that for p ranging from 10 to 65, the error does not change much for different τ values. And as expected, the error decays exponentially as a function of p , e.g., the method exhibits spectral convergence in p . As a result, in the following numerical tests,

we will fix $\tau = 0.1$.

We now move to the error dependence on the truncation order p and the Fibonacci number F_2 used in the numerical integration. Here we will focus on a challenging case by taking $r_s = 0.95$, i.e., the charge is very close to the interface. The results are shown in Fig. 3. First, we observe that for different values of p , the error converges very soon as F_2

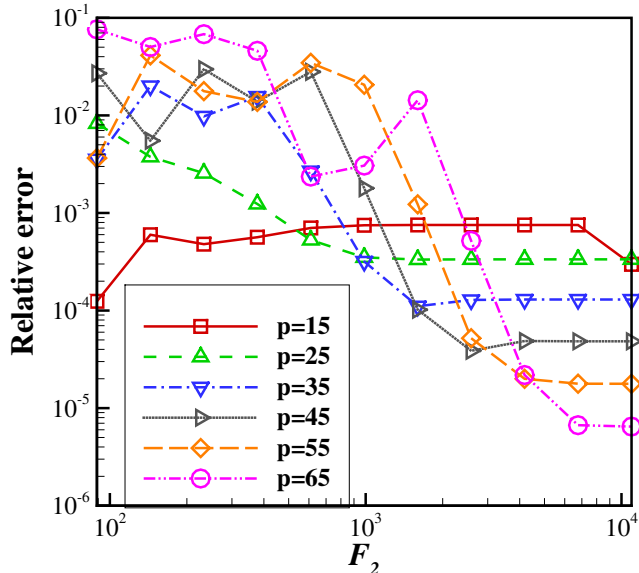


FIG. 3: Absolute error in the self energy as a function of the Fibonacci number F_2 , with truncation order p ranging from 15 to 65. We fix the charge location to be $r_s = 0.95$ and $\tau = 0.1$.

increases due to the high-order convergence of the Fibonacci integration scheme, e.g., for the case $p = 65$, the error saturates if we take $F_2 \geq 6765$. Second, as long as we use sufficient large value for F_2 , the magnitude of the saturated error is decided by the truncation order p we choose. For the case $r_s = 0.95$, if one wants to achieve 5-digits accuracy, then we need to choose $p \sim 55$. Finally, we also compare the HSMA with the original Kirkwood series solution with the same truncation order p . As is shown in Fig. 4, we observe that HSMA can obtain much better accuracy than the Kirkwood series expansion with the same value of p . For example, HSMA with $p = 20$ achieves even better accuracy than the Kirkwood series with $p = 40$ over the whole range of $r_s \in [0.9, 0.98]$. Moreover, by choosing $p = 20$ for HSMA, it is guaranteed that the absolute error remains less than 10^{-2} , while the Kirkwood series can not achieve the same goal even if we take $p = 60$. Thus the HSMA has a clear

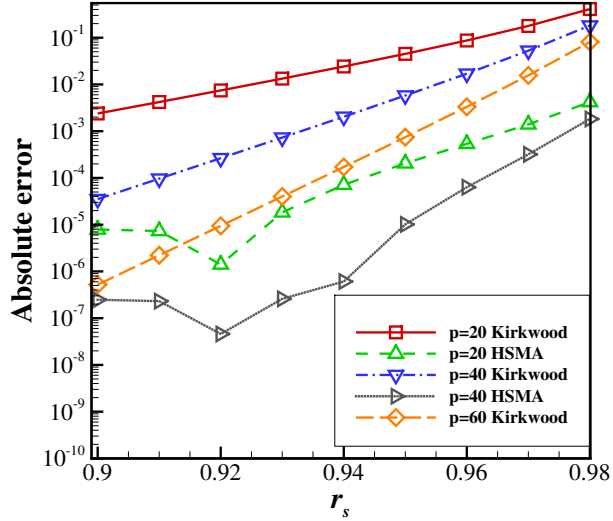


FIG. 4: Absolute errors in the self energy as a function of the source charge location $r_s \in [0.9, 0.98]$ with different values of p , results from both HSMA and Kirkwood series expansion are shown for comparison. Here we fix $F_2 = 1597$.

advantage in terms of accuracy compared with the Kirkwood series approach.

B. CPU time tests

Here we test the CPU time performance of our method for a large number of source charges inside the dielectric sphere. We use FMM (the software package FMM3DLIB [41]) to accelerate the pairwise Coulomb summations, with the FMM precision fixed to be 10^{-6} . The timing results are obtained on a 64-core workstation (4 AMD operation Processors Model 6272, 2.1 GHz with 16 cores each), and we use 32 cores for each run. The parameters of the HSMA are chosen to be $\tau = 0.1, p = 20, F_1 = 987$ and $F_2 = 1597$. As was tested in Sec. IV A, the parameters chosen here are sufficient to obtain numerical error less than 10^{-5} if $r_s < 0.93R$. In the numerical tests here, we randomly generate N source charges inside the dielectric sphere, with N ranging from 10^3 to 10^6 , and we calculate the reaction potential of the system. As is shown in Fig. 5, We find that HSMA accelerated by FMM can achieve linear $\mathcal{O}(N)$ scaling. And compare with the direct sum, the break-even is around $N = 1000$. For large-scale simulations, say if the system contains 10^6 source charges, the CPU time of the HSMA accelerated by FMM is 24s, while with direct sum the cost

becomes 8.9×10^4 s. Thus the FMM-accelerated HSMA can be very attractive for large-scale simulations of charged particles immersed in electrolytes.

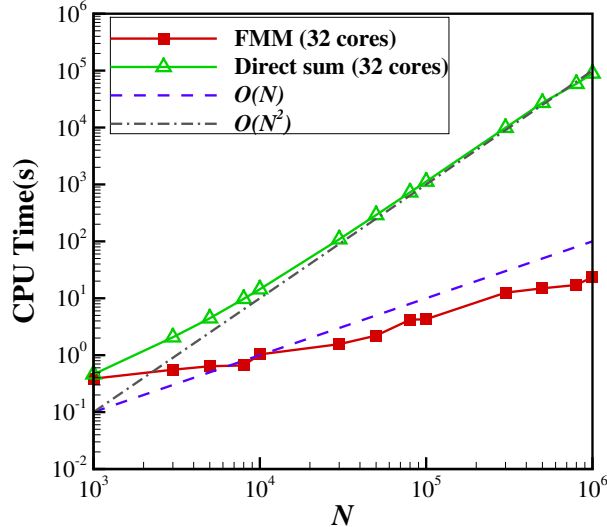


FIG. 5: CPU time for calculating the reaction potential of N random generated point charges, with N ranging from 10^3 to 10^6 . The results of HSMA both with and without FMM acceleration are shown here for comparison. The parameters of HSMA chosen here are $\tau = 0.1$, $P = 20$, $F_2 = 1597$.

V. CONCLUSION

In conclusion, we have developed the harmonic surface mapping algorithm for calculating the reaction potential of a dielectric sphere immersed in electrolytes. Starting from the Kirkwood series solution, we first use the asymptotic expansion to rewrite the reaction potential into the sum of Kelvin images, line images and an extra correction term. Then an auxiliary surface is introduced, by using the Green's second identity, we are able to transform the correction term into an integral on the auxiliary surface. Further combined with the Fibonacci integration scheme, we are finally able to rewrite the reaction potential into a simple Coulomb sum of image charges, which can be further accelerated by FMM in large-scale simulations to achieve linear scaling. Numerical tests demonstrate that HSMA can achieve much better accuracy comparing with the Kirkwood series solution. Particularly, even when a source charge is very close to the dielectric interface, the HSMA can still

obtain ~ 4 digits accuracy with moderate value of p , owing to the analytical resolving of singularity with the image charge expression. Thus the HSMA can be a useful tool for large-scale simulations of charged systems under the hybrid model.

In the future, we plan to implement the HSMA on GPUs to speed up its performance. Another goal is to implement the method in Molecular Dynamics simulations of charged many-body systems. And we are also interested in the application of the HSMA method in the study of relevant physical/biological systems.

Acknowledgements

The authors acknowledge the financial support from the National Natural Science Foundation of China (Grant Nos. 11571236 and 21773165) and the HPC center of Shanghai Jiao Tong University. Z. G. is supported by NSF grants DMS-1418966 and DMS-1819094.

-
- [1] B. Honig and A. Nicholls, *Science* **268**, 1144 (1995).
 - [2] L. Lue and P. Linse, *J. Chem. Phys.* **135**, 224508 (2011).
 - [3] F. B. Sheinerman, R. Norel, and B. Honig, *Curr. Opin. Struct. Biology* **10**, 153 (2000).
 - [4] P. T. Cummings and A. A. Chialvo, *J. Phys.: Condens. Matter* **8**, 9281 (1996).
 - [5] D. Bashford and D. A. Case, *Annu. Rev. Phys. Chem.* **51**, 129 (2000).
 - [6] A. J. Bordner and G. A. Huber, *J. Comput. Chem.* **24**, 353 (2003).
 - [7] Z.-Y. Wang and Z. Ma, *J. Chem. Theory Comput.* **12**, 2880 (2016).
 - [8] Z. Gan, S. Jiang, E. Luijten, and Z. Xu, *SIAM J. Sci. Comput.* **38**, B375 (2016).
 - [9] I. N. Derbenev, A. V. Filippov, A. J. Stace, and E. Besley, *J. Chem. Phys.* **145** (2016).
 - [10] M. Ma, Z. Gan, and Z. Xu, *Phys. Rev. Lett.* **118**, 076102 (2017).
 - [11] R. M. Levy and E. Gallicchio, *Annu. Rev. Phys. Chem.* **49**, 531 (1998).
 - [12] P. Koehl, *Curr. Opin. Struct. Biol.* **16**, 142 (2006).
 - [13] B. Roux and T. Simonson, *Biophys. Chem.* **78**, 1 (1999).
 - [14] M. Feig and C. L. Brooks III, *Curr. Opin. Struct. Biol.* **14**, 217 (2004).
 - [15] N. A. Baker, *Curr. Opin. Struct. Biol.* **15**, 137 (2005).
 - [16] A. Onufriev, *Annu. Rep. Comput. Chem.* **4**, 125 (2008).

- [17] A. Okur and C. Simmerling, *Annu. Rep. Comput. Chem.* **2**, 97 (2006).
- [18] A. Okur, L. Wickstrom, M. Layten, R. Geney, K. Song, V. Hornak, and C. Simmerling, *J. Chem. Theory Comput.* **2**, 420 (2006).
- [19] M. E. Davis and J. A. McCammon, *Chem. Rev.* **90**, 509 (1990).
- [20] F. Fogolari, A. Brigo, and H. Molinari, *J. Mol. Biol.* **15**, 377 (2002).
- [21] N. Baker, *Methods Enzymol* **383**, 94 (2004).
- [22] Y. C. Zhou, M. Feig, and G. W. Wei, *J. Comput. Chem.* **29**, 87 (2008).
- [23] J. G. Kirkwood, *J. Chem. Phys.* **2**, 351 (1934).
- [24] C. Tanford and J. G. Kirkwood, *J. Am. Chem. Soc.* **79**, 5333 (1957).
- [25] C. Neumann, in *Hydrodynamische Untersuchungen: Nebst einem Anhang über die Probleme der Elektrostatik und der magnetischen Induktion* (Teubner, Leipzig, 1964), pp. 279–282.
- [26] W. Cai, S. Deng, and D. Jacobs, *J. Comput. Phys.* **223**, 846 (2007).
- [27] L. Greengard and V. Rokhlin, *J. Comput. Phys.* **73**, 325 (1987).
- [28] L. Greengard and V. Rokhlin, *Acta Numer.* **6**, 229 (1997).
- [29] H. Cheng, L. Greengard, and V. Rokhlin, *J. Comput. Phys.* **155**, 468 (1999).
- [30] L. Ying, G. Biros, and D. Zorin, *J. Comput. Phys.* **196**, 591 (2004).
- [31] S. Deng and W. Cai, *Commun. Comput. Phys.* **2**, 1007 (2007).
- [32] Z. Xu, S. Deng, and W. Cai, *J. Comput. Phys.* **228**, 2092 (2009).
- [33] Z. Xu, Y. Liang, and X. Xing, *SIAM J. Appl. Math.* **73**, 1396 (2013).
- [34] Y. Liang, Z. Xu, and X. Xing, *New J. Phys.* **17**, 083082 (2015).
- [35] Q. Zhao, J. Liang, and Z. Xu, *J. Chem. Phys.* **149**, 084111 (2018).
- [36] J. D. Jackson, *Classical Electrodynamics (3rd Edition)* (John Wiley & Sons, New York, 2001).
- [37] M. Abramowitz and I. A. Stegun, *Handbook of Mathematical Functions with Formulas, Graphs, and Mathematical Tables* (Dover, New York, 1964).
- [38] Z. Xu and W. Cai, *SIAM Rev.* **53**, 683 (2011).
- [39] J. Hannay and J. Nye, *J. Phys. A: Math. Gen.* **37**, 11591 (2004).
- [40] N. A. Gumerov and R. Duraiswami, *J. Comput. Phys.* **272**, 307 (2014).
- [41] *Fmmlib3d software suite*, <http://www.cims.nyu.edu/cmcl/fmm3dlib/fmm3dlib.html>.